High-pressure behaviour of zoisite

High-pressure behaviour of zoisite

MATTEO ALVARO[1,2], ROSS J. ANGEL[1,3], and FERNANDO CÁMARA[4]

[1] Virginia Tech Crystallography Laboratory, Department of Geosciences, , Virginia Polytechnic Institute and State University, Blacksburg, VA 24060, USA

[2]Current address: Dipartimento di Scienze della Terra, Università degli studi di Pavia, Via A. Ferrata 1, 27100 Pavia (Italy)

[3]Current address: Dipartimento di Geoscienze, Università degli studi di Padova, via G. Gradenigo 6, 35131 Padova (Italy)

[4]Dipartimento di Scienze Mineralogiche e Petrologiche, via Valperga Caluso 35 - 10125 Torino (Italy)

Email: matteo.alvaro@gmail.com

Key words: zoisite, high-pressure, X-ray diffraction, compressibility, OH, water, hydrous minerals.

Formatted: Italian (Italy)

ABSTRACT

A high-pressure single-crystal X-ray diffraction (XRD) study has been carried out on two natural zoisite samples $Ca_2Al_{3-x}Fe_xSi_3O_{12}OH$, one Fe-free ($x$ = 0) and Fe-rich (x = 0.12) . The unit-cell parameters were determined for the Fe-free sample at 18 different pressures up to 7.76 GPa and for the Fe-rich sample at 13 different pressures up to 7.63 GPa. The $P(V)$ data for both of the samples were fitted by a third-order Birch-Murnaghan equation of state (BM3 EoS). The equation of state coefficients are: V_0 = 903.39(5) Å^3, K_{T0} = 122.1(7) GPa and K_0' = 6.8(2) for the Fe-free sample and V_0 = 906.95(5) Å^3, K_{T0} = 119.1(7) GPa and K_0' = 7.3(2) for the Fe-rich sample. This shows that the addition of Fe in to the crystal structure of zoisite leads to a slight softening of the structure.

Both compositions exhibit axial compressibilities $\beta_c > \beta_a >> \beta_b$, with the compressibilities of the *a* and *b* axes of the two samples being indistinguishable. The softening of the bulk modulus of zoisite with Fe content follows from softening of the *c*-axis of the structure. A high-pressure structural study of the Fe-free sample showed that the main compression mechanisms in the structure are the compression of ~~the~~soft inter-octahedral distance along [001] and soft intra-octahedral distances along [010] directions, while along [100] the main compression occurs because of the compression of ~~the~~ stiff intra-octahedral distances. The substitution of Fe on to the *M3* octahedral site of the structure leads to an increase of the intra-octahedral distance of the *M3* that triggers the rotation of *M12* and therefore leads to the softening of the *M12* inter-octahedral distances that accounts for the softening of the *c*-axis of the structure.

INTRODUCTION

Several authors (i.e. Forneris and Holloway, 2003; Kirby et al. 1996) have argued that the correct model for explaining the generation of many volcanisme ~~are~~ and intermediate earthquakes in subduction zones involves the progressive dehydration of the subducting slab through a series of reactions that release H_2O into the mantle wedge. These fluids released from subducting slabs could trigger hydration-driven partial melting reactions, inducing partial melting of the mantle wedge above the slab, which in turn is considered responsible for the intermediate earthquakes (i.e. Peacock, 2001 and Kirby et al. 1996), as well as for arc volcanism (i.e. Forneris and Holloway 2003) in subduction zones. A key role in these dehydration reactions is played by the hydrous mineral phases that are mainly contained in the subducting slab. Therefore a detailed study of the properties of the hydrous phases, and especially the thermo-elastic behavior, will be an important requirement for understanding properties and processes within subduction zones, in particular for constraining their stability and the related dehydration reactions in which they are involved as a function of pressure and temperature (i.e. Hacker et al. 2003 and Mao et al. 2007). Minerals of the epidote group for example, participate in numerous relevant phase equilibria, which need to be accurately evaluated in order to understand these geological processes. Zoisite belongs to the epidote group and occurs in high and ultrahigh-pressure metamorphic rocks from a wide variety of geological settings, including continental collisions and subduction zones (i.e. Hacker et al. 2003; Mao et al. 2007 and Enami et al. 2004).

Zoisite is the only member of the epidote group that is orthorhombic, instead of monoclinic. The structure of zoisite (Figure 1) was firstly determined by Fesenko et al. (1955), Fesenko et al. (1956), and was later refined by Dollase (1968). Monoclinic epidotes, including clinozoisite, have two distinct edge-sharing octahedral chains that run along [010]. Zoisite has only one type of octahedral chain parallel to [010] built up of edge sharing octahedra designated *M12* and occupied by Al^{3+} (Ghose and Tsang, 1971). That chain of octahedra~~l~~ is decorated by a second octahedral site, *M3*, which can be occupied by both Al^{3+} and Fe^{3+} (Ghose and Tsang 1971). This site is more distorted and is attached to *M12* octahedra by edge sharing. The octahedral chains are linked by isolated SiO_4 tetrahedra (*T3*) in the **c** direction and by Si_2O_7 groups (*T1* and *T2*) in the **a** and **c** directions (see Fig. 1). In this framework of interconnected octahedral chains and bridging tetrahedra there are two distinct irregularly shaped, sevenfold-coordinated cavities (*Ca1* and *Ca2*) occupied by Ca. Hydrogen is bonded to oxygen O10 which coordinates cations in the octahedral chains (Franz and Liebscher 2004).

Field Code Changed
Field Code Changed
Field Code Changed
Field Code Changed
Field Code Changed
Field Code Changed
Field Code Changed
Field Code Changed
Field Code Changed
Field Code Changed
Field Code Changed
Field Code Changed
Field Code Changed

Several authors have measured the equation of state of zoisite by means of X-ray diffraction on samples with different composition and have obtained several different values for the bulk moduli; 125.1(2.1) GPa was measured by Grevel et al. (2000) on a synthetic zoisite sample with composition $Ca_2Al_3Si_3O_{12}OH$; 127(4) GPa was measured by Pawley et al. (1998) on a natural zoisite sample containing 2.3-4.3% of ferric end member; and 102(7) GPa was obtained by Comodi and Zanazzi (1997) on a zoisite sample with composition $Ca_2Al_2(Al_{0.9}Fe_{0.1})Si_3O_{12}OH$. Recently Mao et al. (2007) measured the elastic constants at ambient conditions by Brillouin scattering on a Fe-free crystal of zoisite from Merelani Hills, to obtain a value of K_{S0} = 125.3(4) GPa which, however, is not in agreement with the compression studies, as we discuss below.

Field Code Changed

In order to clarify the discrepancies among the literature data, and to determine the effect of the substitution of Fe on the bulk modulus, we investigated the high pressure behavior of two samples with different Fe contents, Fe-free (X_{ps}=0) and Fe-rich (X_{ps}=0.12) up to 7.76 and 7.63 GPa respectively, by means of single-crystal X-ray diffraction. We determined the unit-cell parameter evolution on both samples in order to calculate the equation of state and we measured intensity data on the Fe-free sample to follow the evolution of the structure with pressure.

EXPERIMENTAL METHODS

Samples

Two single crystals of natural zoisite with general formula $Ca_2(Al,Fe)_3Si_3O_{12}(OH)$, and different Fe contents were selected. The Fe-free (X_{ps}=0) sample is from the Merelani Hills in the Arusha Region, United Republic of Tanzania (Barot and Boehm 1992) and was kindly provided by A. Zanetti. The Fe-rich sample (X_{ps}=0.12) is from Carinthia, Austria (sample number 8952 from the Museo di Mineralogia, Dipartimento di Scienze della Terra, Pavia, Italy).

Field Code Changed

Electron microprobe analysis

Chemical analyses were performed on different crystals from the same samples that X-ray data collection~~s~~ and structure refinement~~s~~ at ambient conditions showed had very similar structural parameters. ~~Analysis~~ Analyses of the Fe-free sample (X_{ps} = 0) sample ~~are~~ is from Cámara et al.

(2011). A Cameca-Camebax electron microprobe with a fine-focused beam (1 μm diameter) operating in the wavelength-dispersive (WDS) mode was used. Operating conditions were 20 kV accelerating voltage and 20 nA beam current for for Al, Si, K, Ca and Fe and 20 kV and 40 nA for Na, Mg, Ti, V, Mn, Sr, La and Ce, with a beam diameter of 20 μm. The following standards were used (spectral line, analyzing crystal): Amelia albite (Na*K*α, TAP), wollastonite (Ca*K*α, PET), diopside (Si*K*α, TAP), MgO (Mg*K*α, TAP), orthoclase (K*K*α, PET) $MnTiO_3$ (Mn*K*α and Ti*K*α, PET), vanadinite (V*K*α, LIF), Fe_2O_3 (Fe*K*α, LiF), corundum (Al*K*α, TAP), celestine (Sr*L*α, PET), and REE glass 3 (La*L*α and Ce*L*α, LIF). WDS scans showed the absence of fluorine. Data were corrected using the PAP method of Pouchou and Pichoir, (1984). The empirical formulae of our zoisite samples are $(Ca_{1.99}Sr_{0.01})(Al_{2.99}V_{0.01})$ $[Si_2O_7][SiO_4]O(OH)$ and $(Ca_{1.99}Sr_{0.01})(Al_{2.88}Fe_{0.12})$ $[Si_2O_7][SiO_4]O(OH)$, ~~respectively~~ with the OH content being assumed by stoichiometry as the crystals are fluorine-free (Table 1).

Field Code Changed

High-pressure experiments

Two crystals, one Fe-free (size 0.150 × 0.100 × 0.080 mm), and one Fe-rich (size 0.110 × 0.090 × 0.060 mm) were selected for the high-pressure study on the basis of their size, optical sharp extinction, absence of twinning, and X-ray diffraction profiles. The Fe-free and Fe-rich crystals were loaded in two different ETH-type diamond-anvil cells (DACs, Miletich et al. 2000) using a steel gasket (T301) pre-indented to a thickness of 100 μm and with a hole of 250 μm in diameter for both the experiments. A single crystal of quartz was used as an internal diffraction pressure standard (Angel et al. 1997) and a 4:1 mixture of methanol:ethanol was used as pressure medium, which remains hydrostatic throughout the pressure range investigated in this work (Angel et al. 2007). The unit-cell parameters were determined by single-crystal X-ray diffraction using a Huber four-circle diffractometer (non-monochromatised Mo-*K*α radiation) operating at 50 kV and 40 mA, automated

Field Code Changed

Field Code Changed

Field Code Changed

by the SINGLE software (Angel and Finger 2011). The unit cell parameters were measured at 18 different pressures up to ~7.76 GPa for the Fe-free sample and at 13 different pressures, up to ~7.63 GPa, for the Fe-rich sample by centering not less than 20 reflections in the 2θ range between 10° and 30° for each high-pressure data point. Typical half-widths of reflections were between 0.05° and 0.08° in ω and no broadening was detected at any pressure. Full details of the instrument and the peak-centering algorithms are provided by Angel et al. (1997). During the centering procedure the effects of crystal offsets and diffractometer aberrations were eliminated from refined peak positions by the eight-position centering method of King and Finger (1979). Unconstrained unit-cell parameters, obtained by vector least-squares (Ralph and Finger 1982), were found to be similar, within one estimated standard deviation, to the symmetry-constrained ones which are reported in Table 2.

Intensity data for structural refinements were collected simultaneously for the Fe-free crystal on an Xcalibur-1 Oxford Diffraction diffractometer equipped with a point detector (kappa-geometry, graphite-monochromatised Mo-*K*α radiation). Integrated intensity data were then corrected for absorption effects due to the crystal and the DAC using the ABSORB computer program (Burnham 1966; Angel 2004).

All the structure refinements were performed with the SHELX-97 software (Sheldrick, 2008), starting from the atomic coordinates of Cámara et al. (2011). Because of the complexity of the structure and the limited number of observations, all of the refinements were performed with isotropic displacement parameters for all atoms. Details of the structure refinement, bond distances and angles are reported in Tables 3 and 4. Atomic coordinates and displacement parameters are listed in Table 5 (deposited), and *CIF*s are deposited.

Field Code Changed
Field Code Changed
Field Code Changed
Field Code Changed
Field Code Changed
Field Code Changed
Field Code Changed

RESULTS AND DISCUSSION

Elastic behavior

The evolution of the unit-cell parameters and unit-cell volume of the two crystals measured in this study as a function of pressure is shown in Figure 2, along with the previously-published data. All of the unit cell parameters undergo a strong non-linear decrease up to 7.77 GPa and 7.63 GPa for the Fe-free and Fe-rich samples respectively (Figure 2 a, b, c, d and Table 2). Over this pressure range the *a*, *b* and *c* lattice parameters decrease by 1.07 %, 1.90 and 2.29% respectively for the Fe-free sample and by 1.03, 1.89 and 2.33% respectively for the Fe-rich sample. The unit-cell volume decreases non-linearly at an average rate of 6.06 $Å^3$/GPa for the Fe-free sample and 6.13$Å^3$/GPa for the Fe-rich sample. The compression of all of the unit cell parameters is accompanied by significant stiffening of the *b* and *c* axes while the *a* axis shows marginal softening. The lattice parameter variation of both of the samples follows the same compressibility scheme, and for both the compression is completely reversible, with no indication of any change in elastic behavior upon decompression , but for the Fe-free sample there is significant scatter in the *f*-*F* plots of the unit-cell parameters in the pressure range 4-4.5 GPa (Figure 3). This appears to be associated with a subtle change in the structural evolution with pressure, as there is no discontinuity in the *P*-*V* curve nor is there a change in the slope of the *f*-*F* plot of the volume compression (Figure 3d) at this pressure (see discussion).

The *P*(*V*) data were fitted, for both Fe-free and the Fe-rich sample, by a third-order (BM3-EoS) Birch-Murnaghan equation of state (Birch 1947), using the EOSFIT-5.2 software (Angel, 2000). The EoS coefficients of the two samples are reported together in Table 6. The values of the bulk modulus ($K_{T0Fe\text{-}free}$ = 122.1(7) GPa and $K_{T0Fe\text{-}rich}$ = 119.1(7) GPa), and its first pressure derivative ($K''_{Fe\text{-}free}$ =6.8(2) and $K'_{Fe\text{-}rich}$ =7.3(2)) are both in excellent agreement with those indicated by the normalised stress F_E – Eulerian strain f_E plot as shown in Figure 3 (Angel, 2000; $F_E = P/3f_E(1+2f_E)^{5/2}$, $f_E = [(V_0/V)^{2/3}-1]/2$). The bulk moduli obtained from isothermal hydrostatic

Field Code Changed
Field Code Changed
Field Code Changed

compression measurements such as those reported here correspond to the Reuss bound on the isothermal bulk modulus. The values of the elastic moduli tensor of end-member zoisite (Mao et al. 2007) yield a value of the Reuss bound of the adiabatic modulus of 121.6(4) GPa which, using their value for the factor (1+αγT) of 1.016, corresponds to an isothermal bulk modulus of 119.7(4) GPa, which is in between our values. The apparent agreement reported by Mao et al. (2007) between their Brillouin data and the previous compression studies of Grevel et al. (2000) and Pawley et al. (1998) was an artifact of Mao et al. (2007) incorrectly using the VRH average modulus instead of the Reuss bound as a basis for comparison with hydrostatic compression experiments. The slightly higher value of K_{T0} = 125(2) for end-member zoisite obtained by Grevel et al. (2000) is probably a consequence of their fixing the value of *K*' to 4. Considering the data scatter in the other published studies (Figure 2) agreement with any EoS parameters derived from them is fortuitous, and depends on the assumptions made about constraining other EoS parameters such as V_0 and *K*'.

Field Code Changed
Field Code Changed
Field Code Changed
Field Code Changed
Field Code Changed
Field Code Changed

The axial compressibilities at room pressure for *a*, *b*, and *c* (Table 7) were obtained using a parameterised form of the BM3-EoS, in which the individual axes are cubed, following the procedure implemented in the EoS-FIT5.2 software (Angel 2000). Note that the resulting moduli given by EosFit (Table 7) must be multiplied by a factor of 3 to obtain the linear moduli equal to the inverse of the linear compressibilities defined as $\beta_{l0} = \frac{-1}{l}\left(\frac{\delta l}{\delta P}\right)_{P=0}$ which is in turn equal to the sum of the three compressional terms in the elastic compliance matrix for the axis. Thus, for example, the compressibility of the *a*-lattice parameter of zoisite is given by $\beta_1 = s_{11} + s_{12} + s_{13}$. The resulting linear compressibilities for the Fe-free sample in this study (Table ~~8~~7) agree within the uncertainties with those determined from the individual values of the compliance matrix inverted from the c_{ij} values given by Mao et al. (2007). The compressibility scheme is $\beta_a << \beta_b < \beta_c$ for both samples, (β_a:β_b:β_c = 1.00:2.29:2.74 for the Fe-free sample and ~~$\beta_a << \beta_b < \beta_c$ (~~β_a:β_b:β_c = 1.00:2.34:2.99 for the Fe-rich sample) with ***a*** being the most rigid direction and ***c*** the softest. Although the compressibility scheme shows the same general pattern for both samples, and the

Field Code Changed

compressibilities of the ***a*** and ***b*** directions do not change between the two, the increased Fe content leads to a significant softening of ***c*** , and it is this axial softening that results in the reduction of bulk modulus with the addition of Fe to the structure. The same general pattern of axial compressibilities is apparent in the previous experimental studies (Figure 2), although the compressibility of ***a*** was significantly over-estimated by Pawley et al. (1998) and no meaningful values of the linear compressibilities can be obtained from those data.

Structure evolution with pressure

In order to better understand the reasons of the change in the compressibility of zoisites with Fe content, and why the biggest change in compressibility is along the *c*-axis, in the following section we describe briefly the structural evolution of the Fe-free crystal with pressure. The compression of the bond lengths and bond angles at the bridging oxygen atoms alone is not sufficient to explain either the compression mechanism in each direction, nor the strong anisotropy of the structure itself. Therefore, distortion of the polyhedra and their cooperative rotations are the key to explain the main mechanisms that control the average compression of the whole structure.

a) Framework compression

During the pressure increase from room pressure up to 7.77GPa the *a*-axis undergoes a compression of about 0.17 Å. The [100] direction is the least compressible of the whole structure with a bulk modulus of 244(5) GPa for the Fe-free sample and 248(4) for the Fe-rich one. The *M3* octahedra share one oxygen atom (O8) with *T1* tetrahedra on one side while on the other side they share one edge (O1 – O4) with *M12* octahedra, which also share an oxygen atom (O3) with *T1* tetrahedra (see Figures 1a, b and c). These polyhedral linkages follow the path of the 2_1 screw axes running parallel to [1 0 0] (Figure 1b) and therefore they span one half of the unit cell length (*a*/2) which compresses by 0.085 Å over the pressure range studied. The contribution to the compression from the rotation and compression of *M12* and *M3* octahedra is equal to the shortening and rotation

of the vector along the O8 – O5 (O8 shared between *T1* and *M3* and O5 shared between ~~*T1*~~ *T3* and *M12* (0.008 Å)) and the one of the vector O5 – O3 (0.028 Å). The rotation of the *M3* and *M12* octahedra relative to one another shortens the *M3* – *M12* cation – cation distance by 0.033 Å, and results in significant compression of the *T3* tetrahedra (from 2.236 Å^3 to 2.142Å^3, see Table 4 and Figure 4) and increase of the distortion (the volume distortion parameter of Makovicky and Balić Žunić, (1998) increases from 1.43 to 1.94%) of the *T3* tetrahedron (see Table 4 and Figure 5). The largest contribution from the framework to the shortening along [100] actually comes from the shortening and rotation of the O3- O8 edge of the *T1* tetrahedron that contributes ~~as~~ 0.051 Å which also leads to a significant increase in distortion of the tetrahedra.

Formatted: Font: Italic

Field Code Changed

The lengths of the O-O edges shared between the consecutive *M12* octahedra forming continuous chains along the [010] direction (see Figure 1c) are considerably shorter (by 0.2 – 0.3 Å) than the unshared edges, indicating significant cation-cation repulsion between the octahedral cations. One might therefore expect that the [010] direction would be the stiffest direction in the structure. That it is not indicates that compression and/or deformation of the octahedra is important in the compression of the structure. Each octahedron is related to the next in the chain by a mirror plane perpendicular to *b* (shown in Figure 1c with a solid line), and therefore the compression of *b*/2 along ½[010] must be accommodated within a single octahedron. Under compression to 7.6 GPa the opening of the O5-M12-O10 and O6-M12-O4 angles (by 1.4° and 0.25° respectively), together with the shortening of the bond distances M12-O5 (by 0.033Å), ~~the~~ M12-O10 (by 0.015Å), ~~the~~ M12-O4 (by 0.0028Å) and ~~the~~ M12-O6 (by 0.043Å) are the main mechanisms of compression and contribute the total of 0.053 Å to the shortening of each octahedron along [010] (see Table 4 and Figure 6). The individual chains of *M12* octahedra are linked to one another through parallel chains of alternating *M3* octahedra and *T3* tetrahedra (Figure 1a), which also have to shorten under compression. With increasing pressure the distance between the O2 atoms linked to *M3* decreases by 0.073 Å through a combination of bond shortening and closing of the O2-M3-O2 angle, while

the O2-O2 distance forming the edge of the *T3* tetrahedron shortens by 0.033 Å through bond compression alone.

The octahedral chains in zoisite are softer, along their length, than the AlO_6 edge-sharing octahedral chains of the Al_2SiO_5 polymorphs, in which the direct compression of AlO_6 octahedra results in moduli along the chain directions in excess of 200 GPa in sillimanite and andalusite (Burt et al. 2006), while in kyanite (Yang et al. 1997, Comodi et al. 1997) the linear modulus is still 166 GPa, much greater than in zoisite. In all cases the chains are compressed by shortening Al-O bonds (see Table 8 and Figure 8). The compression of the chains of octahedra must be accommodated by the rest of the structure; therefore the difference in compressibility ~~rise~~ rose from the fact that in andalusite and sillimanite the octahedral chains are better supported by the surrounding structure.

Field Code Changed

Field Code Changed

Field Code Changed

Back to zoisite, the [001] direction is the most compressible of the entire structure with a modulus of 89.1(9) GPa for the Fe-free sample and 83.2(5) GPa for the Fe-rich one. In Figure 1b the horizontal line joining the *M12* sites indicates a pair of sites related by the 2_1 screw axis running along [001]. Therefore their z-coordinates differ by ½ and the compression of the framework along ***c*** must result in the shortening of this *M12-M12* vector, which requires shortening of both the polyhedral links *M12-T3-M12* and *M12-T1-T2-M12*. Within the pressure increase from room *P* to 7.77GPa the biggest contribution to the shortening of *c/2* (0.115Å) in the first link is from the shortening by 0.07 Å of the O5-O6 edge of the *T3* tetrahedron. Most of the compression of this O5-O6 edge (see Figure 9) comes from a decrease in the O5-T3-O6 angle of about 3°, and a small contribution comes from shortening of T3-O5 but not T3-O6 (Figure 7e and Table 4). The rest of the required compression (0.04 Å) comes from shortening of the M12-O5 and M12-O6 bonds (Figure 7a and Table 4). In the parallel polyhedral link the *T1-T2* distance shortens by 0.03 Å (by shortening T2-O9, not by changing the T-O-T angle, see Figure 10 and Table 4). The remaining 0.08Å compression is supplied by the *M12* octahedral rotation together with a small bond distance shortening. The *M12* is rotating around the O atoms shared with *T1* and *T2*, which thus compresses

the *T3* bridge. The different elastic behaviour with composition can be attributed to the contribution of the *M3* polyhedra: compression along [001] can be explained by the softening of the *M3*-O1 bonds, which can become softer in M3 site populated Fe^{3+} (Table 4, Figure 7b).

b) *Extra framework cations contribution*

The distribution of the Ca-O bonds in space (especially with respect to the orientation of the shorter vs the longer bonds) does not give any explanation for the anisotropic behavior of the structure. Looking at the Ca1 site, the shortest of the Ca – O bonds, the Ca1 – O7 ~~bond~~ (oxygen shared with *T2* tetrahedron, see Figure 1b) is the stiffest one and shortens by only 0.0034Å (see Table 4). This bond is sub-parallel to [100] and is opposite to the Ca1 – O6 and Ca1 – O5 (see Figure 1b) that are the longest and softest among the Ca1 – O bonds, with a compression of 0.094Å and 0.061Å respectively (see Table 4). Therefore the combined effect given by those bonds is that the Ca1 cavity shrinks isotropically. In the Ca2 site the stiffest bonds are to the O3 oxygen which is shared with *T1* tetrahedron (Figure 1b) although these are not the shortest bonds. These Ca-O3 bonds lie sub-parallel to [100] and would therefore stiffen ***a*** were it not for the fact that the two Ca2 – O2, which are the longest and softest among the Ca2 – O bonds are also sub-parallel to [100]. As a consequence the combined effect is that the Ca2 cavity, as well as the Ca1 cavity, shrinks almost isotropically.

c) *Hydrogen-bond geometry*

As described above, the Fe-free sample shows significant scatter in the *f-F* plots of the unit-cell parameters in the pressure range 4-4.5 GPa (Figure 3), which is not accompanied by a discontinuity in the *P-V* curve nor is there a change in the slope of the *f-F* plot of the volume compression (Figure 3d). Therefore, this data scatter is unlikely to be associated with the isostructural phase transition that occurs with increasing iron contents (Liebscher et al. 2002) as that transition leads to an *increase* in volume compared to that of the end-member composition, and so is not expected to occur upon compression. Nevertheless, it is worth noting that there is a sharp

Field Code Changed

increase of distortion of the *T1* polyhedron (Figure 5b) and a discontinuity in the O7-O9-O8 angle (Figure 11) between 4 and 5 GPa. A close inspection of the O10...O4 distance (with the O4 anion being the acceptor of the hydrogen bond in zoisite structure) shows that there is a consistent reduction of this distance in the room-*P* to 4-5 GPa pressure range (up to 0.2 Å, Figure 12a). The same is observed for the O10...O2 distance, which remains unchanged up to 4 GPa, and then ~~start~~begin ~~-~~decreasing. If we combine shortening of these distances with the behaviour of the *T1* tetrahedron we can infer that something is happening to the hydrogen bonding topology. Quite likely, the H atom is ~~getting~~ going off of the O4...O10 junction and ~~start~~ begin to form~~ing~~ a bifurcated bond with O2. This change in bonding topology must be instantaneous and would explain the softening in **c** lattice parameter and the hardening in **b** lattice parameter (Figures 3b and c).

CONCLUSIONS

We have shown that the addition of Fe to the structure of pure zoisite results in a slight decrease in the bulk modulus which is the result of a softening of the ***c*** axis. The pattern of pressure-induced strains and the structural evolution at high pressure is also similar to the high-temperature behavior measured by Cámara et al. (2011) on an Fe-free crystal from the same sample studied in this work. At high temperatures, in the *T* range from 303K to 770K, the *a* lattice parameter shows negative thermal expansion (NTE) and shortens by 0.018Å, while *b* and *c* lattice parameters expand during the temperature increase by 0.076Å and 0.150Å respectively. The anisotropy of the elastic response of zoisite to pressure and temperature is therefore ~~close~~ related. In both cases the *c* lattice parameter shows the biggest variation, being the softest direction at high-*P* (with a bulk modulus of $K_{T0cFe\text{-}free}$= 89.1(9)GPa) and at high-*T* it is the direction of greatest expansion, with a thermal expansion coefficient of $\alpha^{\circ}_{33(1bar,298K)}$ = 18.95(2)·$10^{-6}K^{-1}$ (Cámara et al. 2011). The *a* lattice

Field Code Changed

parameter is the stiffest direction at high-*P* (with a bulk modulus of $K_{T0cFe\text{-}free}$= 244(5)GPa) and at high-*T* it shows negative thermal expansion ($\alpha^{\circ}_{11(1bar,298K)}$ = -1.18(3)·$10^{-6}K^{-1}$, Cámara et al. 2011). The *b* lattice parameter has a bulk modulus close to that of *c* at high-*P* ($K_{T0bFe\text{-}free}$= 105(2)GPa) and a thermal expansion coefficient also close to *c* ($\alpha^{\circ}_{22(1bar,298K)}$ = 17.31(2)·$10^{-6}K^{-1}$ Cámara et al. 2011). The reasons for this anisotropy can be found in the linkage system of the framework. Along the [001] direction, the compression occurs mainly by shortening of the inter-polyhedral distances (see Figure 6), and is therefore certainly bigger with respect to the compression along [100] and [010] that is achieved by compression of the intra-polyhedral distances (see Figure 7) and rotation of the polyhedra with respect one to another.

The compressibility behavior is also affected by the Fe-contents at the *M3* site. As reported by Cámara et al. (2011) the thermo-elastic parameters of the unit-cell volume of zoisite obtained in their study compared with those of a natural epidote previously reported by Gatta et al. (2011) with higher Fe contents [*i.e.* $Ca_{1.925}Fe_{0.745}Al_{2.265}Ti_{0.004}Si_{3.037}O_{12}(OH)$] showed significant differences, being α_{Vo} = 5.93(5)·10^{-5} K^{-1} for zoisite and 5.1(2) ·10^{-5} K^{-1} for epidote. Therefore, compearing two slightly different structures (epidote and zoisite) it ~~appears~~ sems that at high-*T*, higher Fe contents reduce the volume thermal expansion coefficient (Cámara et al. 2011); however several high temperature data on zoisite sample with different Fe contents (Camara pers. Comm.), clearly showed that the volume thermal expansion coefficient increases with increasing the Fe contents. This is clearly in agreement with the high-*P* behavior showed by our data for all the lattice parameters, where the higher the Fe contents the lower the bulk modulus, as showed in Figure 2d and Table 6.

The key to understand this behavior can be found in the evolution of the structure with increasing ~~the~~ Fe content~~s~~. As reported by Liebscher et al. (2002), and confirmed by our data, increasing Fe content causes an increase in the volume of the *M3* octahedron while the other polyhedral volumes remain practically constant (Liebscher et al. 2002). The increase in volume of

Field Code Changed

Field Code Changed

Field Code Changed

Field Code Changed

Field Code Changed

the *M3* is accommodated by increasing the distance between the cation and the apical oxygens (O4 – O8, see Figure 1a) together with the *M3* – O1 bond lengths (see Figure 1a and b). The increase of the O4 – O8 distance causes both a regularization and a rotation of the *M3* octahedra together with a rotation (by 0.5°) and regularization of the *M12* octahedra (Liebscher et al. 2002). The increase of the O4 – O8 distance along *a* together with the rotation of *M3* is compensated by rotation of the *T2* tetrahedra around the relatively fixed apical O3 atom of the *M12* octahedron. The rotation of *T2* leads to rotation of the corner-linked *T1* tetrahedron in the opposite direction, which is reflected by the increasing O8-O9-O7 angle of the Si_2O_7 group. Therefore, an increase in the Fe content has essentially the same effect on the tilt of *T1* and *T2* tetrahedra as increasing pressure that opens the O8 – O9 – O7 (see Figure 11). Therefore, this mechanism of rotation of *T1* and *T2* tetrahedra that takes place with increasing Fe content softens the [001] direction by making the relative rotation of *T1* and *T2* tetrahedra even easier, while the increase in the distance O4 – O8 together with the rotation of *M12* stiffens the [100] direction. In addition, the increase of the *M3* – O1 bond lengths with increasing Fe content is a further mechanism that softens the [001] direction.

Field Code Changed

Acknowledgements

M. Alvaro and R.J. Angel were supported by NSF grant EAR 0738692 to NL Ross and RJ Angel. R. Gastoni (CNR – IGG, Pavia, Italy) is thanked for preparing the sample. A. Fioretti and R. Carampin (CNR – IGG, Padova, Italy) are thanked for their assistance during the microprobe analyses.

References

Angel, R.J. (2000) Equations of state. In R.M. Hazen and R.T. Downs, Eds., Reviews in Mineralogy: High temperature and high pressure crystal chemistry, 41, p. 117–211. Mineralogical Society of America, Washington, D.C.

Angel, R.J. (2004) Absorption corrections for diamond-anvil pressure cells implemented in the software package - ABSORB6.0. Journal of Applied Crystallography, 37, 486-492.

Angel, R.J., Allan, D.R., Milletich, R., and Finger, L.W. (1997) The use of quartz as an internal pressure standard in high-pressure crystallography. Journal of Applied Crystallography, 30, 461-466.

Angel, R.J., Bujak, M., Zhao, J., Gatta, G.D., and Jacobsen, S.D. (2007) Effective hydrostatic limits of pressure media for high-pressure crystallographic studies. Journal of Applied Crystallography, 40, 26-32.

Angel, R.J., and Finger, L.W. (2011) SINGLE: A program to control single-crystal diffractometers. Journal of Applied Crystallography, 44(1), 247-251.

Barot, N., and Boehm, E. (1992) Gem-quality green zoisite. Gems & Gemology, 28(1), 4-15.

Birch, F. (1947) Finite elastic strain of cubic crystals. Physical Review, 71(11), 809.

Burnham, C.W. (1966) Computation of absorption corrections and the significance of end effects. American Mineralogist, 51, 159–167.

Burt, J.B., Ross, N.L., Angel, R.J., and Koch, M. (2006) Equations of state and structures of andalusite to 9.8 GPa and sillimanite to 8.5 GPa. American Mineralogist, 91(2-3), 319-326.

Cámara, F., Gatta, G.D., Meven, M., and Pasqual, D. (2011) Thermal expansion and high temperature structure evolution of zoisite by single-crystal X-ray and neutron diffraction.

Comodi, P., and Zanazzi, P.F. (1997) The pressure behavior of clinozoisite and zoisite: An X-ray diffraction study. American Mineralogist, 82(1), 61-68.

Comodi, P., Zanazzi, P.F., Poli, S., and Schmidt, M.W. (1997) High-pressure behavior of kyanite: Compressibility and structural deformations. American Mineralogist, 82(5), 452-459.

Dollase, W.A. (1968) Refinement and comparison of the structures of zoisite and clinozoisite. American Mineralogist, 53, 1882 - 1898.

Enami, M., Mizukami, T., and Yokoyama, K. (2004) Metamorphic evolution of garnet-bearing ultramafic rocks from the Gongen area, Sanbagawa belt, Japan. Journal of Metamorphic Geology, 22(1), 1-15.

Fesenko, E., Rumanova, I., and Belov, N. (1955) The crystal structure of zoisite. Structure Reports, 19, 464–465.

Fesenko, E., Rumanova, I., and Belov, N. (1956) The crystal structure of zoisite. Structure Reports, 20, 396-398.

Forneris, J.F., and Holloway, J.R. (2003) Phase equilibria in subducting basaltic crust: Implications for H_2O release from the slab. Earth and Planetary Science Letters, 214(1-2), 187-201.

Gatta, G.D., Merlini, M., Lee, Y., and Poli, S. (2011) Behavior of epidote at high pressure and high temperature: A powder diffraction study up to 10 GPa and 1,200 K. Physics and Chemistry of Minerals, 1-10.

Ghose, S., and Tsang, T. (1971) Ordering of V^{2+}, Mn^{2+}, and Fe^{3+} ions in zoisite, $Ca_2Al_3Si_3O_{12}(OH)$. Science, 171(3969), 374-376.

Grevel, K.-D., Nowlan, E.U., Fasshauer, D.W., and Burchard, M. (2000) In situ X-ray diffraction investigation of lawsonite and zoisite at high pressures and temperatures. American Mineralogist, 85(1), 206-216.

Hacker, B.R., Peacock, S.M., Abers, G.A., and Holloway, S.D. (2003) Subduction factory 2. Are intermediate-depth earthquakes in subducting slabs linked to metamorphic dehydration reactions? Journal of Geophysical Research, 108(B1), 2030.

King, H.E., and Finger, L.W. (1979) Diffracted beam crystal centering and its application to high-pressure crystallography. Journal of Applied Crystallography, 12(Aug), 374-378.

Kirby, S.H., Stein, S., Okal, E.A., and Rubie, D.C. (1996) Metastable mantle phase transformations and deep earthquakes in subducting oceanic lithosphere. Review of Geophysics, 34(2), 261-306.

Liebscher, A., Gottschalk, M., and Franz, G. (2002) The substitution Fe^{3+}-Al and the isosymmetric displacive phase transition in synthetic zoisite: A powder X-ray and infrared spectroscopy study. American Mineralogist, 87(7), 909-921.

Makovicky, E., and Balić Žunić, T. (1998) New measure of distortion for coordination polyhedra. Acta Crystallographica Section B, 54(6).

Mao, Z., Jiang, F., and Duffy, T.S. (2007) Single-crystal elasticity of zoisite $Ca_2Al_3Si_3O_{12}$ (OH) by Brillouin scattering. American Mineralogist, 92(4), 570-576.

High-pressure single-crystal techniques. In R.M. Hazen and R.T. Downs, Eds., High-Temperature and High-Pressure Crystal Chemistry, 41, p. 445–519. Reviews in Mineralogy and Geochemistry, Mineralogical Society of America, Chantilly, Virginia.

Pawley, A.R., Chinnery, N.J., and Clark, S.M. (1998) Volume measurements of zoisite at simultaneously elevated pressure and temperature. American Mineralogist, 83, 1030-1036.

Peacock, S.M. (2001) Are the lower planes of double seismic zones caused by serpentine dehydration in subducting oceanic mantle? Geology, 29(4), 299-302.

Pouchou, J., and Pichoir, F. (1984) Un nouveau modèle de calcul pour la microanalyse quantitative par spectrométrie de rayons X. La Recherche Aérospatiale, 3(167), 92.

Ralph, R.L., and Finger, L.W. (1982) A computer-program for refinement of crystal orientation matrix and lattice-constants from diffractometer data with lattice symmetry constraints. Journal of Applied Crystallography, 15(Oct), 537-539.

Sheldrick, G.M. (2008) A short history of SHELX. Acta Crystallographica Section A, 64, 112-122.

Formatted: English (U.S.)

Yang, H., Hazen, R.M., Finger, L.W., Prewitt, C.T., and Downs, R.T. (1997) Compressibility and crystal structure of sillimanite, Al_2SiO_5, at high pressure. Physics and Chemistry of Minerals, 25(1), 39-47.

Figures

Figure 1

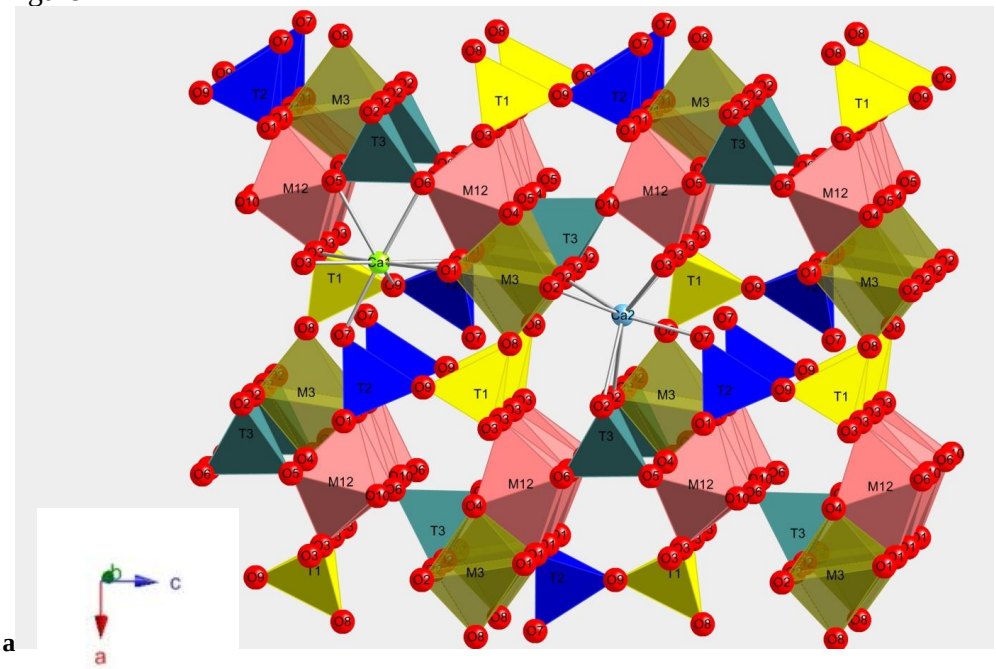

a

b

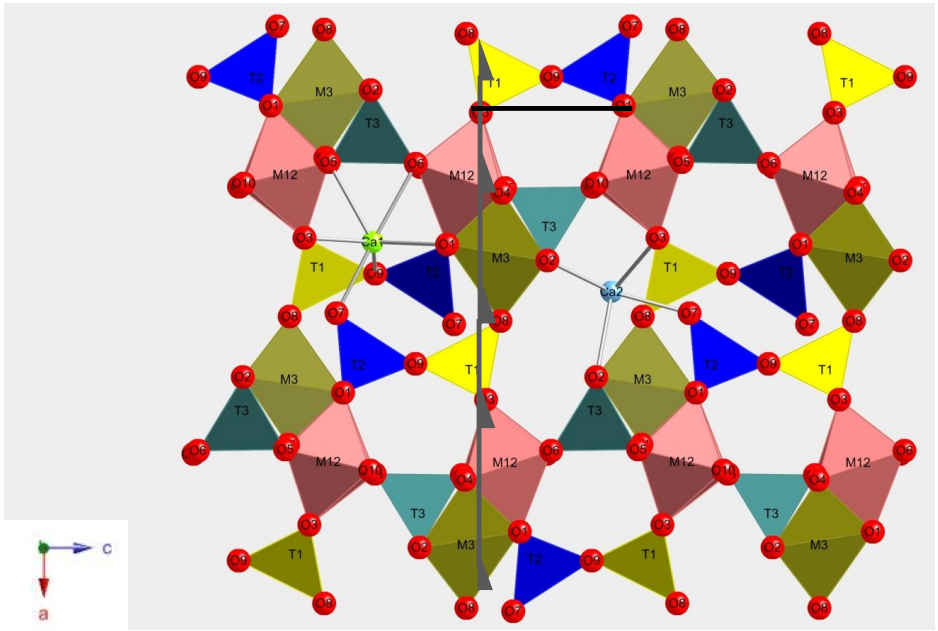

c

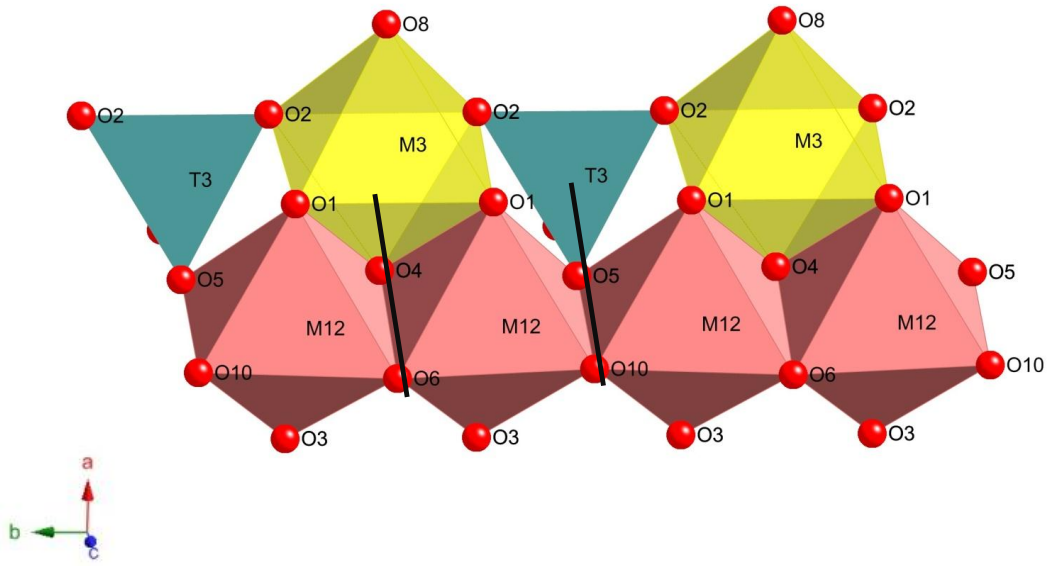

Figure 1. Schematic view of the structure along different crystallographic directions: (a) along *b* lattice tilted to show the direction of the octahedra chain going along *b* direction.; (b) along *b*

lattice, with over imposed the 2_1 screw axis running along [1 0 0] and the black line joining a pair of M12 sites related by a 2_1 screw axis running alon [0 1 0]; (c) inclined along *c* lattice direction showing the mirror plane (black slid line) relating the M12 sites.

Figure 2

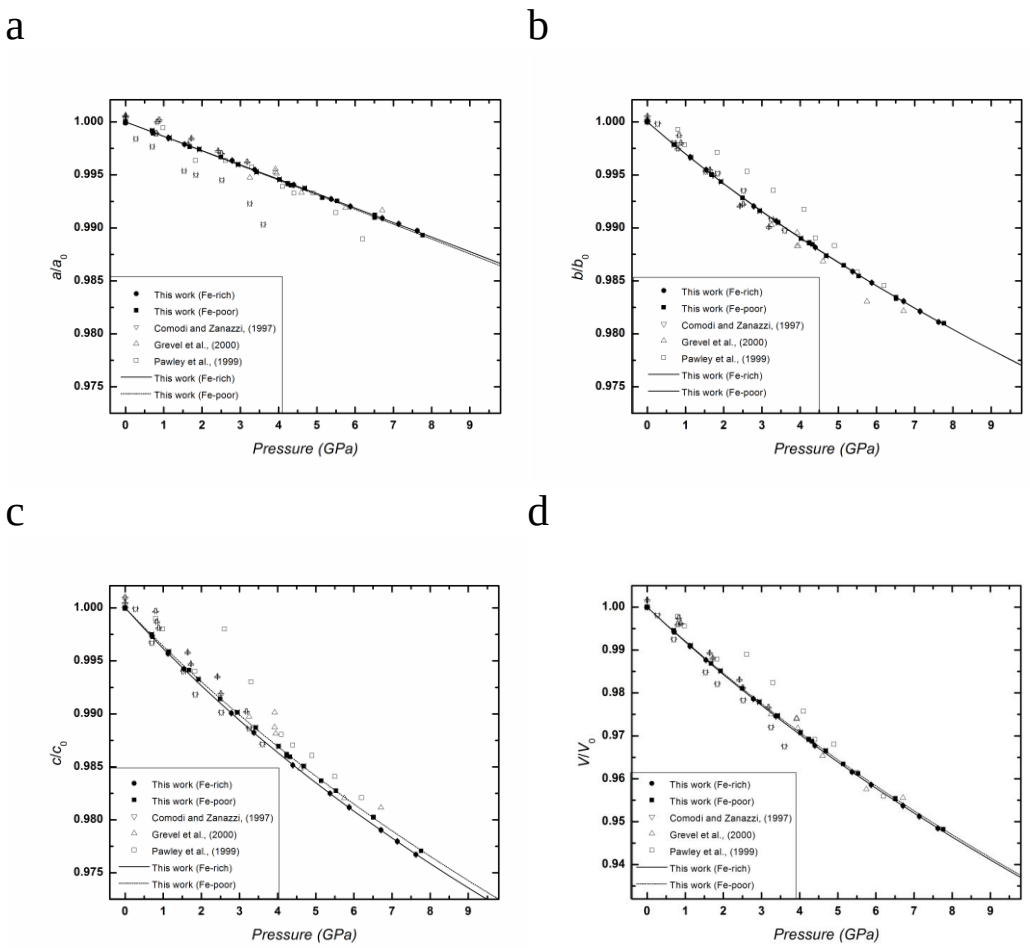

Figure 2. Evolution of the unit cell parameters as a function of pressure: (a) a/a_0; (b) b/b_0;(c) c/c_0 and (d) V/V_0 unit-cell parameters as a function of pressure for the samples Fe-free (filled squares), Fe-rich (filled circles), data by Comodi and Zanazzi, (1997) (open inverted triangle) Pawley et al., (1998) (open square) and Grevel et al., (2000) (open triangle).

Figure 3

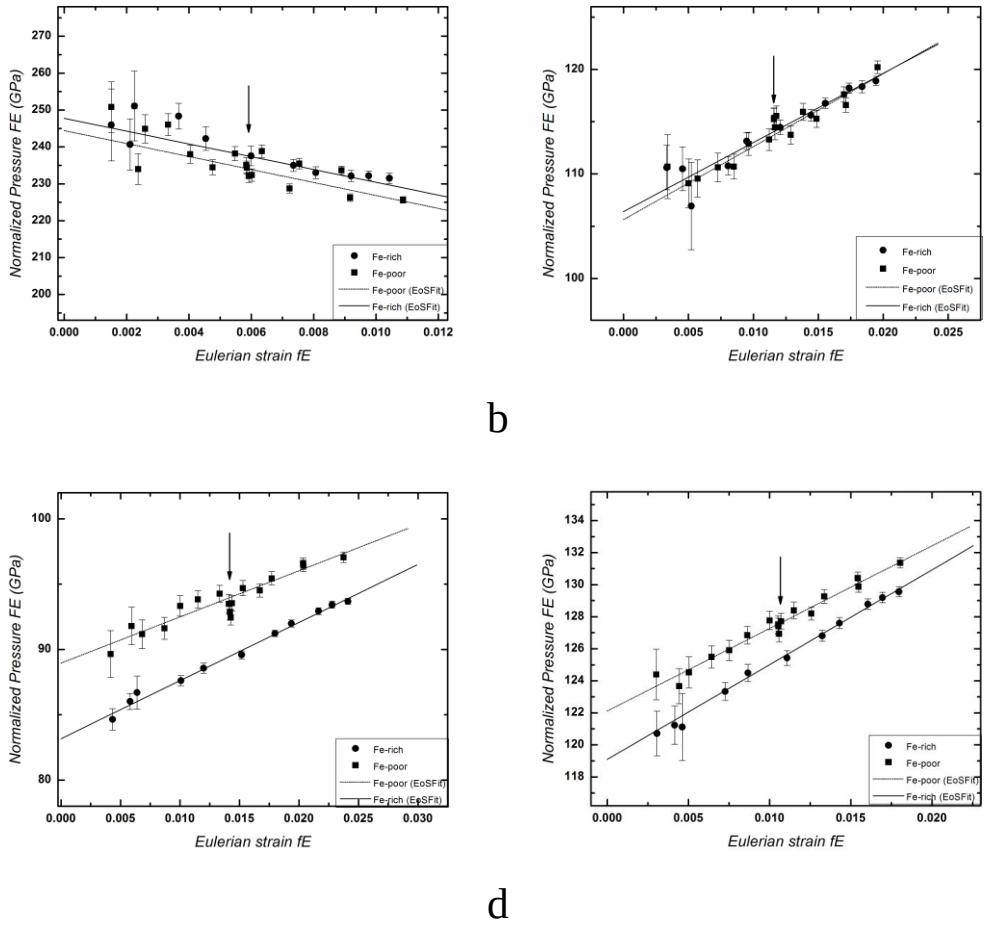

Figure 3. F_E-f_E plot for the (a) *a* lattice parameter, (b) *b* lattice parameter, (c) *c* lattice parameter and (d) unit cell volume.

Figure 4

a

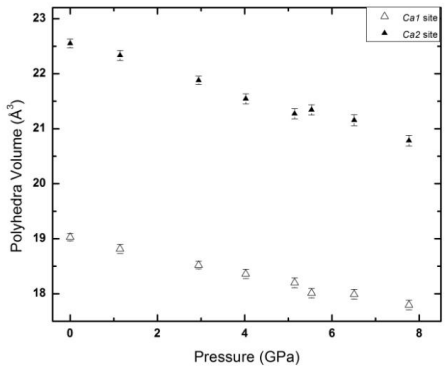

b

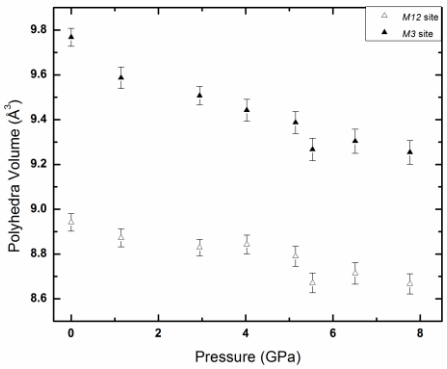

c

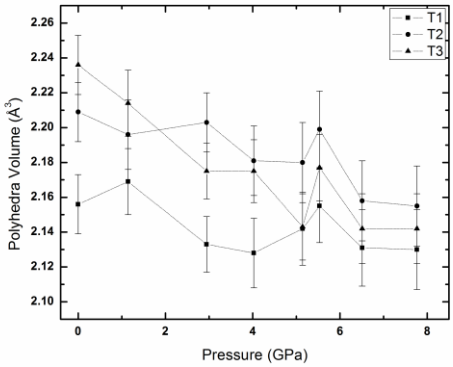

Figure 4. Evolution of the volumes of the polyhedra with increasing pressure: (a) *Ca1* and *Ca2* sites (open and filled triangles respectively); (b) *M12* and *M3* sites (opene and filled triangles respectively); (c) *T1*, *T2* and *T3* (squares, circles and triangles respectively).

Figure 5

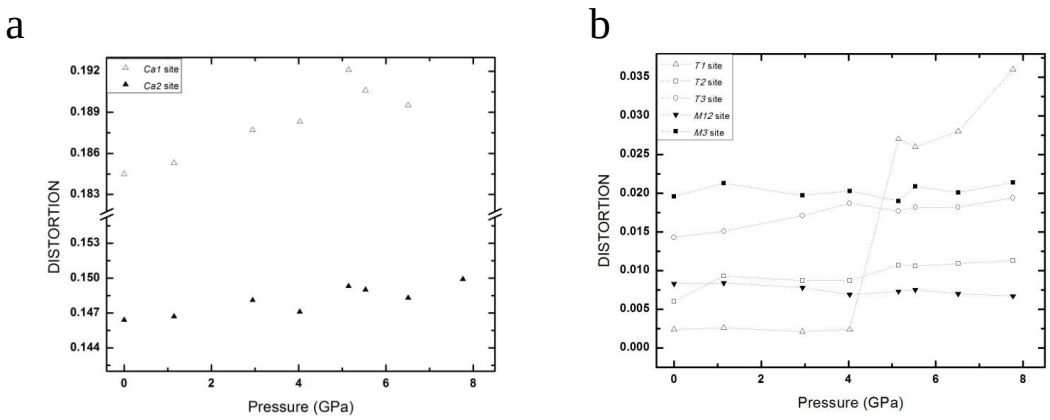

Figure 5. Variation of the polyhedra distortions with pressure. (a) *Ca*1 and *Ca*2 sites (open triangle and filled triangle respectively); (b) *T*1, *T*2, *T*3, *M*12, *M*3 (open triangle, filled triangle, open inverse triangle, filled inverse triangle and open square respectively).

Figure 6

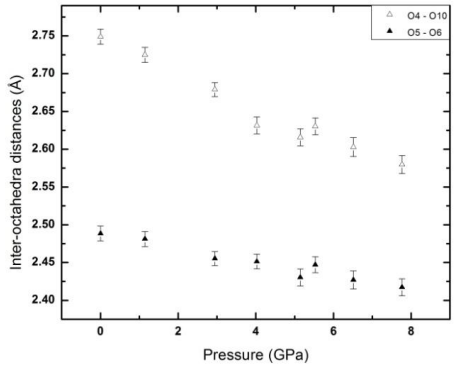

Figure 6. Inter-octahedra distances O4-O10 (open triangle) and O5-O6 (filled triangle).

Figure7

a

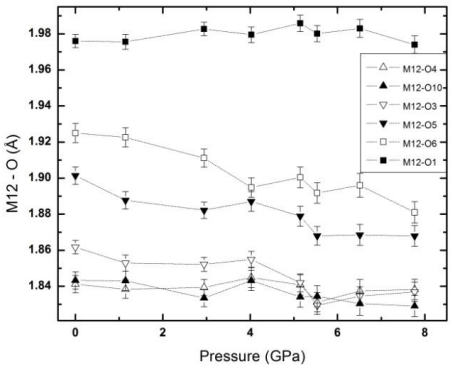

b

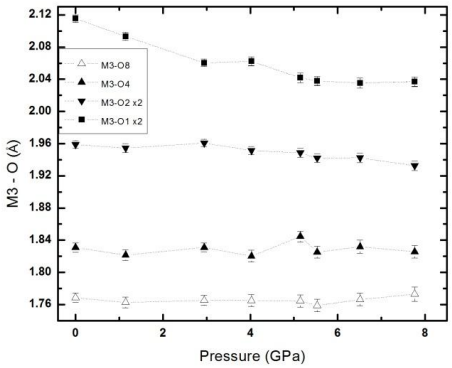

c

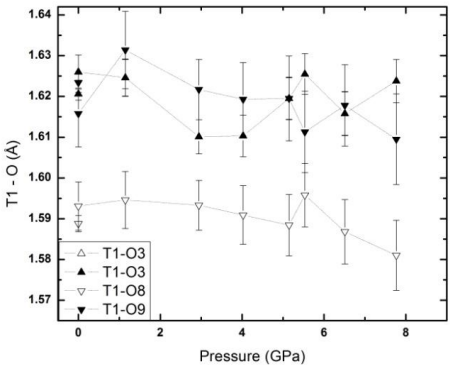

d

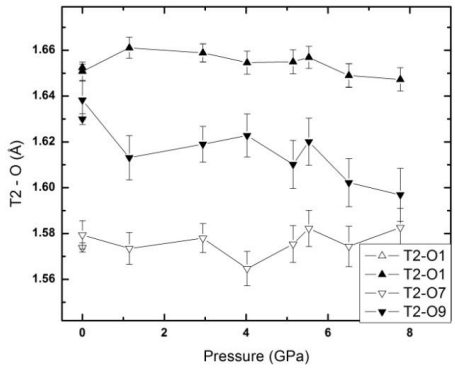

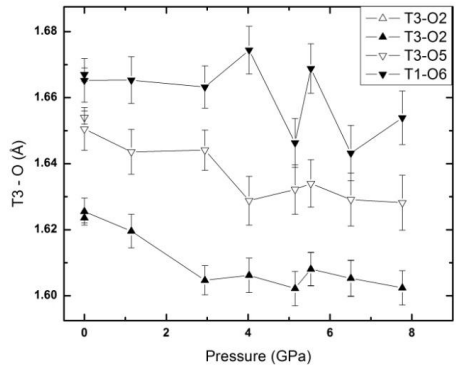

e

Figure 7. Evolution of the *M*12 – O (a), *M*3 – O (b), *T*1 (c), *T*2 (d) and *T*3 (e) bond distances with increasing pressure.

Figure 8

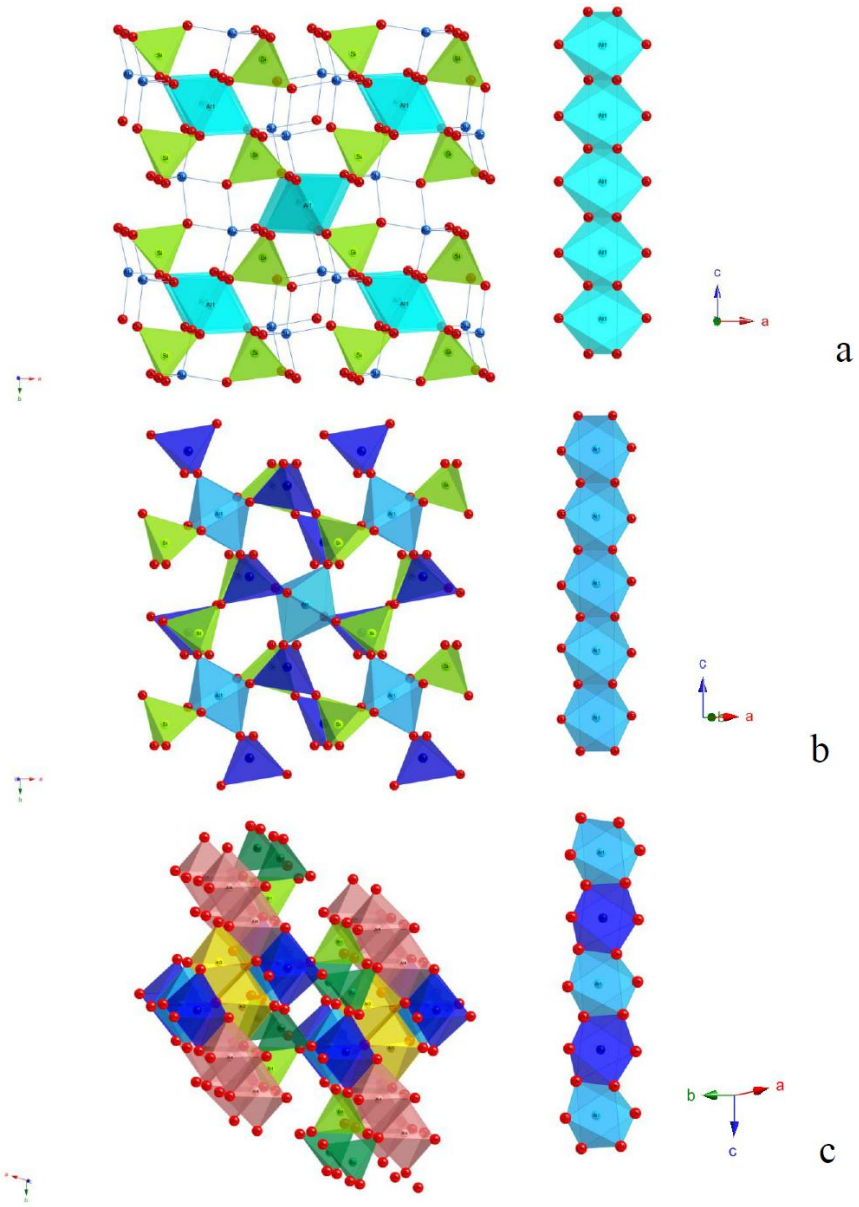

Figure 8. Comparison of the structure of andalusite (a), sillimanite (b) and kyanite (c) showing the difference in the linkage between the octahedra and the different orientation of the chain of octahedra.

Figure 9

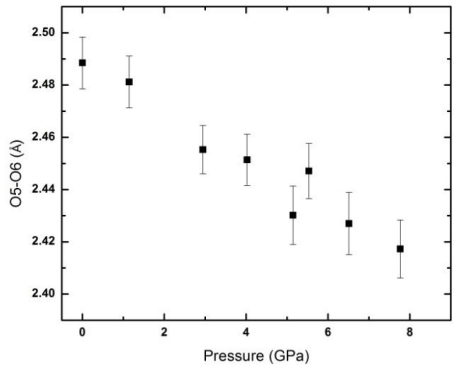

Figure 9. Variation of O5 – O6 distance with *P*.

Figure 10

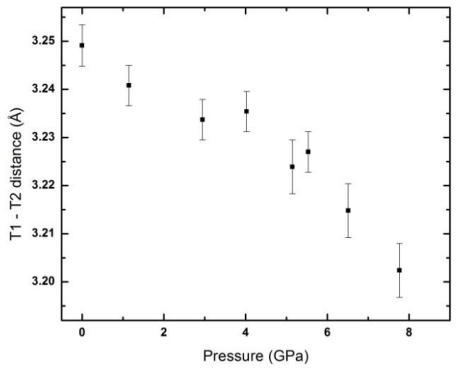

Figure 10. Variation of *T1 – T2* distance with *P*.

Figure 11

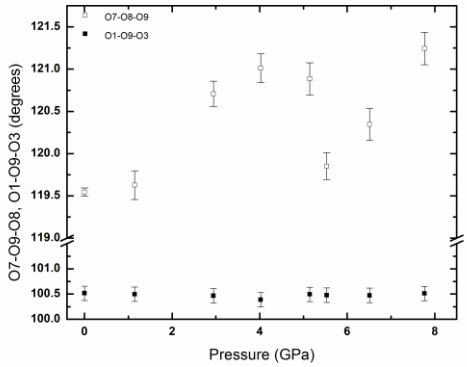

Figure 11. Evolution of the O7 – O9 – O8 and O1 – O9 – O3 angles with increasing pressure.

Figure 12

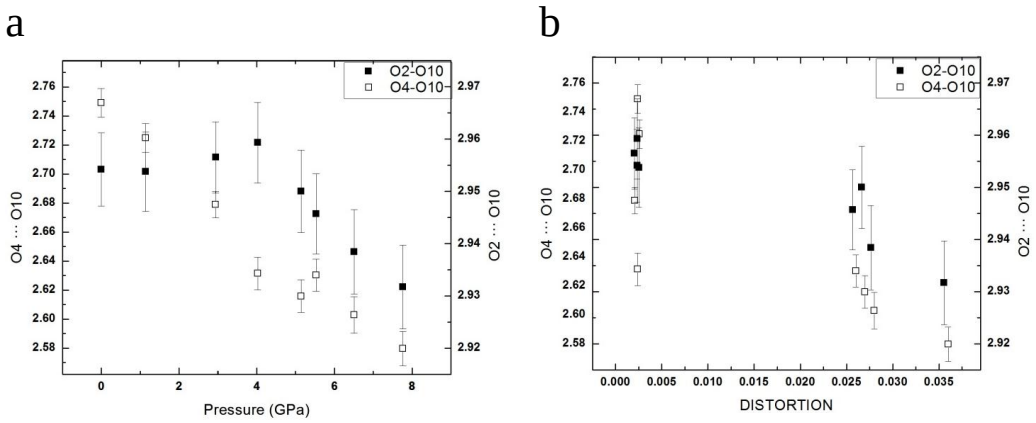

Figure 12. Evolution of the O4 – O10 and O2 – O10 bond distance~~s~~ increasing pressure (a) and with the variations of the *T1* tetrahedron distortion parameter (b) as defined by Makovicky and Balić Žunić, (1998)

Field Code Changed

Tables

Table 1. Mean Zoisite composition of the Fe-free and Fe-rich samples based on the average of 10 point analyses. Formulae are in atoms per formula unit (a.p.f.u.) based on 13 anions. Analysis for the Fe-free sample is from Cámara et al., (2011).

Na_2O	0.01(1)	Na	0.001	Na_2O	0.06(12)	Na	0.009
MgO	0.01(1)	Mg	0.001	MgO	0.04(3)	Mg	0.005
Al_2O_3	33.56(15)	$Al^{(VI)}$	2.986	Al_2O_3	31.83(21)	$Al^{(VI)}$	2.876
SiO_2	39.91(18)	Si	3.014	SiO_2	38.96(15)	Si	2.987
K_2O	0.00(1)	K	0.000	K_2O	0.01(1)	K	0.001
CaO	24.25(16)	Ca	1.962	CaO	24.23(15)	Ca	1.990
TiO_2	0.05(1)	Ti	0.003	TiO_2	0.08(1)	Ti	0.005
V_2O_3	0.15(1)	V	0.009	V_2O_3	0.01(2)	V	0.001
Cr_2O_3	0.00(0)	Cr	0.000	Cr_2O_3	0.00(0)	Cr	0.000
MnO	0.01(1)	Mn	0.000	MnO	0.02(1)	Mn	0.005
Fe_2O_3	0.02(2)	Fe^{3+}	0.001	Fe_2O_3	2.06(22)	Fe^{3+}	0.119
SrO	0.17(5)	Sr	0.008	SrO	0.45(4)	Sr	0.020
La_2O3	0.02(2)	La	0.000	La_2O3	0.02(2)	La	0.000
Ce_2O3	0.02(3)	Ce	0.001	Ce_2O3	0.03(2)	Ce	0.001
H_2O	1.99(1)	H	1.000	H_2O	1.96(1)	H	1.000
Total	**100.16**	**Total**	**8.985**	**Total**	**99.75**	**Total**	**9.015**

Notes: *Calculated assuming 1 a.p.f.u. of H. F was below the detection limit.

Formatted: English (U.S.)

Formatted: English (U.S.)

Formatted: English (U.S.)

Table 2a. Unit-cell parameters at the different pressure values, measured on the Fe-free crystal.

P(GPa)	*a*(Å)	*b*(Å)	*c*(Å)	*V*(Å^3)
0.0001	16.2004 (5)	5.5529 (4)	10.0423 (5)	903.39 (6)
0.697 (5)	16.1869 (5)	5.5411 (4)	10.0169 (6)	898.45 (7)
1.144 (7)	16.1760 (4)	5.5342 (4)	10.0007 (6)	895.27 (6)
1.926 (8)	16.1587 (4)	5.5215 (3)	9.9746 (5)	889.93 (6)
2.945 (7)	16.1353 (4)	5.5063 (3)	9.9432 (5)	883.41 (6)
3.426 (6)	16.1239 (4)	5.5001 (3)	9.9288 (5)	880.51 (6)
4.025 (11)	16.1124 (5)	5.4917 (4)	9.9110 (6)	876.96 (6)
4.685 (12)	16.0988 (5)	5.4827 (3)	9.8921 (6)	873.12 (6)
5.533 (11)	16.0796 (5)	5.4721 (4)	9.8690 (6)	868.36 (6)
6.515 (12)	16.0583 (4)	5.4602 (3)	9.8439 (5)	863.12 (5)
6.511 (8)	16.0540 (4)	5.4609 (4)	9.8437 (6)	863.00 (6)
7.766 (9)	16.0271 (4)	5.4473 (3)	9.8119 (5)	856.63 (6)
5.145 (6)*	16.0845 (4)	5.4777 (3)	9.8785 (6)	870.36 (6)
4.325 (9)*	16.1038 (5)	5.4886 (3)	9.9011 (6)	875.13 (6)
4.243 (8)*	16.1063 (5)	5.4896 (4)	9.9026 (6)	875.56 (7)
4.243 (8)*	16.1054 (5)	5.4897 (3)	9.9020 (5)	875.47 (6)
4.239 (6)*	16.1067 (6)	5.4893 (5)	9.9036 (8)	875.61 (9)
2.496 (5)*	16.1468 (4)	5.5130 (3)	9.9560 (5)	886.26 (5)
1.680 (5)*	16.1623 (5)	5.5253 (4)	9.9833 (7)	891.52 (7)
0.722 (5)*	16.1831 (5)	5.5409 (4)	10.0150 (6)	898.03 (7)
0.0001	16.1992 (4)	5.5529 (4)	10.0420 (6)	903.29 (7)

Note: *data measured during decompression. Standard deviation are given in parenthesis

Table 2b. Unit-cell parameters at the different pressure values, measured on the Fe-rich crystal.

P(GPa)	*a*(Å)	*b*(Å)	*c*(Å)	*V*(Å^3)
0.0001 (0)	16.2095 (6)	5.5654 (2)	10.0536 (2)	906.95 (5)
3.377 (7)	16.1363 (7)	5.5133 (2)	9.9353 (4)	883.88 (6)
4.398 (9)	16.1132 (8)	5.4994 (3)	9.9044 (3)	877.66 (7)
5.375 (7)	16.0916 (5)	5.4868 (2)	9.8776 (3)	872.10 (5)
6.709 (9)	16.0623 (7)	5.4712 (2)	9.8428 (4)	864.98 (6)
7.139 (9)	16.0535 (5)	5.4659 (3)	9.8321 (5)	862.72 (7)
7.626 (10)	16.0430 (7)	5.4603 (2)	9.8196 (4)	860.19 (6)
5.875 (9)*	16.0801 (6)	5.4809 (2)	9.8644 (4)	869.38 (5)
2.785 (5)*	16.1503 (5)	5.5211 (2)	9.9538 (3)	887.55 (5)
1.542 (7)*	16.1753 (8)	5.5402 (4)	9.9958 (2)	895.77 (8)
1.124 (6)*	16.1850 (7)	5.5469 (2)	10.0103 (3)	898.70 (6)
0.0001 (0)*	16.2084 (11)	5.5658 (3)	10.0539 (4)	906.99 (9)

Note: *data measured during decompression. Standard deviations are given in ~~parenthesis~~parentheses

Table 3. Unit-cell parameters and structure refinements results ~~on crystals of crystal~~ for the Fe-free crystal.

P (GPa)	**0.0001**	**1.144(7)**	**2.945(7)**	**4.025(11)**	**5.533(11)**	**6.511(12)**	**7.766(9)**	**5.145(6)***
Label	**P0**	**P2**	**P4**	**P6**	**P8**	**P9b**	**P10b**	**P11d**
~~*a* (Å)~~	~~16.2004(5)~~	~~16.1760(4)~~	~~16.1353(4)~~	~~16.1124(5)~~	~~16.0796(5)~~	~~16.0539(4)~~	~~16.0271(4)~~	~~16.0845(4)~~
~~*b* (Å)~~	~~5.5529(4)~~	~~5.5342(4)~~	~~5.5062(3)~~	~~5.4917(4)~~	~~5.4721(4)~~	~~5.4609(4)~~	~~5.4473(3)~~	~~5.4777(3)~~
~~*c* (Å)~~	~~10.0423(5)~~	~~10.0007(6)~~	~~9.9432(5)~~	~~9.9110(6)~~	~~9.8690(6)~~	~~9.8437(6)~~	~~9.8119(5)~~	~~9.8785(6)~~
~~*V* (Å^3)~~	~~903.40(8)~~	~~895.27(8)~~	~~883.41(7)~~	~~876.96(8)~~	~~868.36(8)~~	~~863.00(8)~~	~~856.63(7)~~	~~870.36(8)~~
space group	*Pnma*	*Pnma*	*Pnma*	*Pnma*	*Pnma*	*Pnma*	*Pnma*	*Pnma*
Z	4	4	4	4	4	4	4	4
Density (calc.) Mg/m^3	3.223	3.252	3.296	3.32	3.353	3.374	3.399	3.345
Absorption coeff.(mm^{-1})	2.03	2.05	2.08	2.11	2.11	2.13	2.14	2.12
Resolution (θ)	2.51 to 29.99°	2.39 to 29.99°	2.41 to 29.96°	2.42 to 29.99°	2.42 to 29.93°	2.43 to 29.99°	2.43 to 29.99°	2.42 to 29.99°
Completeness (%)	66.2	72.3	73.1	72.7	72.4	71.0	71.9	70.8
Extinction coeff	0.015(2)	0.015(2)	0.029(2)	0.035(2)	0.034(2)	0.038(5)	0.038(3)	0.021(2)
n. of *I*/s > 4	591	493	539	459	459	552	421	439
n all	952	1028	1024	1014	1003	1000	990	998
GooF	1.06	0.937	0.923	0.903	0.905	1.023	0.929	0.909
R_{int} (%)	0.059	0.069	0.064	0.086	0.099	0.012	0.101	0.086
R_{4s} (%)	6.20	6.21	5.22	5.40	5.65	7.84	6.58	5.92
R_w (%)	9.25	9.49	10.62	10.51	11.07	14.56	11.14	10.11
$R_w$all (%)	13.7	18.2	14.36	18.79	18.35	16.80	13.61	12.52
*R*all (%)	10.9	11.74	12.25	12.63	13.20	17.04	21.06	20.10
NP†	57	57	57	57	57	57	57	57

Note: * data measured during decompression; † NP = number of refine parameters.

Formatted Table

Table 4. Selected bond lengths (Å) and angles (°) in *Pnma* structures refined with the data from Fe-free crystals.

***P*(GPa)**	**0.0001**	**1.144(7)**	**2.945(7)**	**4.025(11)**	**5.145 (6)***	**5.533(11)**	**6.511(12)**	**7.766(9)**
T1-O3 x2	1.626(4)	1.625(4)	1.610(4)	1.610(5)	1.619(5)	1.625(5)	1.616(5)	1.624(5)
T1-O8	1.593(6)	1.595(7)	1.593(6)	1.591(7)	1.588(7)	1.596(8)	1.587(8)	1.581(9)
T1-O9	1.616(8)	1.631(9)	1.622(7)	1.619(9)	1.619(10)	1.611(10)	1.618(10)	1.609(11)
<T1-O>	1.62(1)	1.62(1)	1.61(1)	1.61(1)	1.61(0)	1.61(1)	1.61(1)	1.61(1)
V_{T1}(Å^3)	2.16(2)	2.17(2)	2.13(2)	2.13(2)	2.14(2)	2.16(2)	2.13(2)	2.13(2)
TQE_{T1}	1.0018	1.0023	1.0016	1.0019	1.0021	1.0022	1.0023	1.0029
TAV_{T1}	7.474	9.586	6.544	7.729	8.34	8.705	9.095	11.528
$T1V_{distortion}$	0.0024	0.0026	0.0021	0.0024	0.027	0.026	0.028	0.036
T2-O1 x2	1.651(4)	1.661(5)	1.659(4)	1.655(5)	1.655(5)	1.657(5)	1.649(5)	1.647(5)
T2-O7	1.579(6)	1.573(7)	1.578(6)	1.565(7)	1.575(8)	1.582(8)	1.574(9)	1.583(8)
T2-O9	1.638(9)	1.613(10)	1.619(8)	1.623(9)	1.610(10)	1.620(10)	1.602(10)	1.597(12)
<T2-O>	1.63(4)	1.63(5)	1.63(4)	1.62(4)	1.62(4)	1.63(4)	1.62(5)	1.62(4)
V_{T2}(Å^3)	2.21(2)	2.20(2)	2.20(2)	2.18(2)	2.18(2)	2.20(2)	2.16(2)	2.16(2)
TQE_{T2}	1.0049	1.0056	1.0049	1.0053	1.0061	1.0065	1.0062	1.0069
TAV_{T2}	16.397	17.543	15.617	16.938	19.703	22.103	20.176	23.462
$T2V_{distortion}$	0.006	0.0093	0.0087	0.0087	0.0107	0.0106	0.0109	0.0113
T3-O2 x2	1.625(4)	1.619(5)	1.605(4)	1.606(5)	1.602(5)	1.608(5)	1.605(5)	1.602(5)
T3-O5	1.650(7)	1.644(7)	1.644(6)	1.629(7)	1.632(7)	1.634(7)	1.629(8)	1.628(8)
T1-O6	1.665(7)	1.665(7)	1.663(6)	1.674(7)	1.646(7)	1.668(7)	1.643(8)	1.654(8)
<T3-O>	1.64(4)	1.64(4)	1.63(4)	1.63(4)	1.62(4)	1.63(4)	1.62(4)	1.62(5)
V_{T3}(Å^3)	2.24(2)	2.21(2)	2.18(2)	2.18(2)	2.14(2)	2.18(2)	2.14(2)	2.14(2)
TQE_{T3}	1.0104	1.0111	1.0131	1.0136	1.0133	1.0135	1.0133	1.0144
TAV_{T3}	40.28	42.851	50.675	51.937	51.788	51.615	51.77	55.568
$T3V_{distortion}$	0.0143	0.0151	0.0171	0.0187	0.0177	0.0182	0.0182	0.0194
M12-O4	1.841(5)	1.838(5)	1.839(4)	1.845(6)	1.841(6)	1.831(5)	1.837(6)	1.838(6)
M12-O10	1.843(5)	1.843(5)	1.833(5)	1.843(5)	1.834(6)	1.834(6)	1.830(6)	1.829(6)
M12-O3	1.862(4)	1.853(4)	1.852(4)	1.855(4)	1.842(5)	1.829(5)	1.835(5)	1.837(5)
M12-O5	1.901(5)	1.888(5)	1.882(4)	1.887(5)	1.879(6)	1.868(5)	1.868(6)	1.868(6)
M12-O6	1.925(5)	1.923(5)	1.911(5)	1.895(5)	1.900(6)	1.892(6)	1.896(7)	1.881(6)
M12-O1	1.976(4)	1.976(4)	1.983(4)	1.979(4)	1.986(5)	1.980(4)	1.983(5)	1.974(5)
<M12-O>	1.89(4)	1.89(4)	1.88(4)	1.88(4)	1.88(4)	1.87(4)	1.88(4)	1.87(4)
V_{M12}(Å^3)	8.94(4)	8.87(4)	8.83(4)	8.84(4)	8.79(5)	8.67(4)	8.71(5)	8.67(5)
OQE_{M12}	1.007	1.0068	1.0067	1.0062	1.0065	1.0069	1.0065	1.0062
OAV_{M12}	20.557	20.218	19.68	18.565	18.98	20.339	18.875	18.479
$M12V_{distortion}$	0.0083	0.0084	0.0078	0.0069	0.0073	0.0075	0.007	0.0067
M3-O8	1.768(6)	1.763(7)	1.765(6)	1.765(7)	1.764(8)	1.759(8)	1.766(8)	1.773(9)
M3-O4	1.831(6)	1.821(7)	1.831(6)	1.820(7)	1.845(7)	1.825(7)	1.832(8)	1.826(8)
M3-O2 x2	1.959(5)	1.954(6)	1.961(5)	1.951(5)	1.949(6)	1.942(5)	1.942(6)	1.933(6)
M3-O1 x2	2.115(5)	2.093(5)	2.060(5)	2.062(5)	2.042(6)	2.038(5)	2.035(6)	2.037(6)

Formatted: English (U.S.)

<M3-O>	1.96(12)	1.95(12)	1.94(12)	1.94(12)	1.93(11)	1.92(11)	1.93(11)	1.92(11)
V_{M3}(Å^3)	9.77(4)	9.59(5)	9.51(4)	9.44(5)	9.39(5)	9.27(5)	9.30(5)	9.25(5)
OQE_{M3}	1.0212	1.0214	1.0191	1.0193	1.0182	1.0192	1.0183	1.0187
OAV_{M3}	48.207	50.718	47.591	47.527	48.284	50.723	48.94	50.78
$M3V_{distortion}$	0.0196	0.0213	0.0197	0.0203	0.019	0.0209	0.0201	0.0214
Ca1-O7	2.261(6)	2.261(7)	2.251 (6)	2.255 (7)	2.262 (8)	2.236 (8)	2.230 (8)	2.257 (8)
Ca1-O3 x2	2.408(5)	2.405(5)	2.399 (4)	2.381 (5)	2.386 (6)	2.385 (5)	2.376 (6)	2.374 (6)
Ca1-O1 x2	2.516(5)	2.502(5)	2.495 (5)	2.489 (5)	2.479 (6)	2.472 (5)	2.471 (6)	2.461 (8)
Ca1-O6	2.558(6)	2.541(7)	2.507 (6)	2.509 (7)	2.499 (7)	2.483 (7)	2.484 (8)	2.464 (6)
Ca1-O5	2.579(6)	2.573(7)	2.557 (6)	2.551 (7)	2.534 (7)	2.542 (7)	2.545 (7)	2.518 (8)
<Ca1-O>	2.46(17)	2.46(17)	2.44 (17)	2.44 (17)	2.43 (18)	2.43 (17)	2.42 (17)	2.42 (18)
V_{Ca1}(Å^3)	19.03(7)	18.81(8)	18.52 (7)	18.36 (8)	18.20 (9)	18.01 (9)	17.99 (9)	17.80 (9)
Ca2-O7	2.301(7)	2.293(8)	2.278 (7)	2.275 (8)	2.254 (8)	2.256 (8)	2.265 (9)	2.222 (9)
Ca2-O3 x2	2.454(4)	2.461(5)	2.453 (4)	2.454 (5)	2.440 (5)	2.452 (6)	2.436 (6)	2.421 (6)
Ca2-O2 x2	2.515(4)	2.507(5)	2.483 (5)	2.465 (5)	2.454 (6)	2.452 (5)	2.451 (6)	2.438 (6)
Ca2-O2 x2	2.794(4)	2.770(5)	2.753 (4)	2.726 (5)	2.727 (5)	2.724 (5)	2.711 (5)	2.709 (5)
<Ca2-O>	2.55(10)	2.54(16)	2.52 (16)	2.51 (16)	2.50 (17)	2.50 (17)	2.49 (16)	2.48 (18)
V_{Ca2}(Å^3)	22.55(8)	22.33(9)	21.88 (7)	21.54 (9)	21.27 (9)	21.34 (9)	21.16 (10)	20.78 (10)
O4···O10	2.749(10)	2.725(10)	2.679(9)	2.632(11)	2.616(11)	2.630(11)	2.603(13)	2.580(12)
O2···O10	2.954(7)	2.954(8)	2.957(7)	2.959(8)	2.950(8)	2.946(8)	2.938(8)	2.932(8)
O5-M12-O10	82.7(2)	83.1(2)	83.1(2)	83.8(2)	83.8(2)	83.9(2)	84.1(2)	84.2(2)
O6-M12-O4	86.1(2)	85.9(2)	86.3(2)	86.4(2)	85.7(2)	85.7(2)	86.4(2)	86.3(2)

Note: TQE, TAV, OQE, and OAV are quadratic elongation and angle variance for tetrahedra and ~~octhaedra~~octahedra (Robinson et al. 1971); polyhedral volumes calculated with IVTON (Balić-Žunić and Vicković, 1996); *Data measured during decompression. Volume distortions ($V_{distortion}$) are calculated as defined by Makovicky and Balić Žunić~~,~~ (1998).

Formatted: English (U.S.)

Formatted: English (U.S.)

Formatted: English (U.S.)

Table 5. Fractional coordinates and displacement parameters obtained with the data from Fe-free crystal.

***P*(GPa)**	**0.0001**	**1.144(7)**	**2.945(7)**	**4.025(11)**	**5.533(11)**	**6.511(12)**	**7.766(9)**	**5.145(6)***
T1x	0.41075(13)	0.41099(15)	0.41048(13)	0.41046(18)	0.41037(18)	0.41005(18)	0.41022(18)	0.41022(16)
y	0.75	0.75	0.75	0.75	0.75	0.75	0.75	0.75
z	0.2828(3)	0.2821(3)	0.2808(3)	0.2798(3)	0.2809(3)	0.2794(4)	0.2793(3)	0.2796(4)
U_{iso}	0.0067(5)	0.0060(6)	0.0103(5)	0.0108(6)	0.0123(7)	0.0113(7)	0.0115(6)	0.0108(7)
T2x	0.08147(13)	0.08098(15)	0.08073(14)	0.08033(18)	0.08034(18)	0.08054(18)	0.08008(18)	0.08005(18)
y	0.25	0.25	0.25	0.25	0.25	0.25	0.25	0.25
z	0.1061(3)	0.1059(3)	0.1057(3)	0.1059(3)	0.1051(3)	0.1054(4)	0.1059(3)	0.1058(4)
U_{iso}	0.0069(5)	0.0065(6)	0.0101(5)	0.0117(7)	0.0110(7)	0.0097(7)	0.0101(6)	0.0119(7)
T3x	0.16030(12)	0.16030(14)	0.16006(13)	0.15964(16)	0.15965(18)	0.16001(16)	0.16003(18)	0.15990(18)
y	0.25	0.25	0.25	0.25	0.25	0.25	0.25	0.25
z	0.4355(3)	0.4349(3)	0.4354(3)	0.4349(3)	0.4353(3)	0.4350(3)	0.4350(3)	0.4356(3)
U_{iso}	0.0056(5)	0.0061(6)	0.0096(5)	0.0111(6)	0.0117(6)	0.0095(6)	0.0105(6)	0.0096(6)
M12X	0.24952(10)	0.24938(11)	0.24930(10)	0.24907(12)	0.24908(12)	0.24907(13)	0.24889(13)	0.24902(13)
Y	0.9971(3)	0.9978(4)	0.9976(3)	0.9975(4)	0.9979(4)	0.9983(4)	0.9986(4)	0.9989(6)
Z	0.1895(2)	0.1895(2)	0.1888(2)	0.1882(2)	0.1885(3)	0.1875(3)	0.1878(2)	0.1873(3)
U_{iso}	0.0066(4)	0.0059(4)	0.0098(4)	0.0104(4)	0.0106(5)	0.0100(5)	0.0106(5)	0.0109(5)
M3X	0.10596(14)	0.10568(18)	0.10561(15)	0.10572(18)	0.1059(2)	0.10516(18)	0.1054(2)	0.1053(2)
Y	0.75	0.75	0.75	0.75	0.75	0.75	0.75	0.75
Z	0.3005(3)	0.3000(3)	0.2994(3)	0.3002(4)	0.2996(4)	0.3000(4)	0.2989(4)	0.2993(4)
U_{iso}	0.0072(5)	0.0068(6)	0.0108(6)	0.0113(7)	0.0127(7)	0.0091(7)	0.0109(7)	0.0113(7)
CA1X	0.36666(11)	0.36624(12)	0.36599(10)	0.36572(13)	0.36573(13)	0.36545(13)	0.36554(13)	0.36544(14)
Y	0.25	0.25	0.25	0.25	0.25	0.25	0.25	0.25
Z	0.4375(2)	0.4370(2)	0.4365(2)	0.4360(2)	0.4363(3)	0.4363(3)	0.4359(2)	0.4359(3)
U_{iso}	0.0109(4)	0.0099(4)	0.0140(4)	0.0145(5)	0.0141(5)	0.0137(5)	0.0137(5)	0.0141(5)
CA2X	0.45185(11)	0.45266(12)	0.45335(11)	0.45397(13)	0.45376(13)	0.45426(14)	0.45466(13)	0.45481(14)
Y	0.25	0.25	0.25	0.25	0.25	0.25	0.25	0.25
Z	0.1150(2)	0.1139(2)	0.1127(2)	0.1118(2)	0.1117(3)	0.1113(3)	0.1109(2)	0.1103(3)
U_{iso}	0.0104(4)	0.0084(5)	0.0122(4)	0.0125(5)	0.0119(5)	0.0112(5)	0.0117(5)	0.0128(6)
O1X	0.1305(2)	0.1302(2)	0.1291(2)	0.1288(2)	0.1281(2)	0.1280(3)	0.1284(3)	0.1280(3)
Y	0.9998(7)	0.9969(8)	0.9951(7)	0.9951(9)	0.9945(8)	0.9931(9)	0.9929(8)	0.9936(9)
Z	0.1465(4)	0.1465(6)	0.1475(4)	0.1471(6)	0.1486(6)	0.1478(6)	0.1469(6)	0.1472(6)
U_{iso}	0.0094(9)	0.0089(10)	0.0116(9)	0.0111(11)	0.0116(11)	0.0131(12)	0.0111(10)	0.0122(12)
O2X	0.1014(2)	0.1013(3)	0.1015(2)	0.1005(3)	0.1015(3)	0.1012(3)	0.1013(3)	0.1009(3)
Y	0.0132(7)	0.0139(9)	0.0147(8)	0.0146(9)	0.0133(9)	0.0140(9)	0.0123(9)	0.0128(11)

Z	0.4302(6)	0.4297(6)	0.4311(4)	0.4314(6)	0.4329(6)	0.4320(6)	0.4313(6)	0.4321(6)
U_{iso}	0.0087(8)	0.0097(9)	0.0131(9)	0.0125(10)	0.0173(11)	0.0148(11)	0.0132(10)	0.0128(11)
O3X	0.3591(2)	0.3588(3)	0.3591(2)	0.3591(3)	0.3580(3)	0.3588(3)	0.3579(3)	0.3584(3)
Y	0.9917(7)	0.9913(8)	0.9912(7)	0.9927(9)	0.9958(8)	0.9948(9)	0.9945(9)	0.9940(9)
Z	0.2452(4)	0.2443(6)	0.2428(4)	0.2430(6)	0.2421(6)	0.2409(6)	0.2406(6)	0.2411(6)
U_{iso}	0.0079(8)	0.0068(9)	0.0115(8)	0.0110(9)	0.0108(10)	0.0137(11)	0.0123(9)	0.0113(10)
O4X	0.2190(3)	0.2183(4)	0.2191(3)	0.2187(4)	0.2195(4)	0.2198(4)	0.2189(4)	0.2194(6)
Y	0.75	0.75	0.75	0.75	0.75	0.75	0.75	0.75
Z	0.3014(7)	0.3011(7)	0.3029(6)	0.3040(8)	0.3032(8)	0.3036(8)	0.3020(8)	0.3033(9)
U_{iso}	0.0077(13)	0.0083(15)	0.0102(13)	0.0131(16)	0.0098(16)	0.0093(16)	0.0084(15)	0.0155(18)
O5X	0.2277(3)	0.2274(4)	0.2275(3)	0.2269(4)	0.2273(4)	0.2277(4)	0.2273(4)	0.2267(4)
Y	0.25	0.25	0.25	0.25	0.25	0.25	0.25	0.25
Z	0.3122(7)	0.3115(7)	0.3115(6)	0.3123(7)	0.3121(8)	0.3119(8)	0.3109(7)	0.3110(8)
U_{iso}	0.0086(13)	0.0057(13)	0.0097(12)	0.0110(15)	0.0123(16)	0.0100(15)	0.0084(15)	0.0072(15)
O6X	0.2718(3)	0.2714(4)	0.2701(3)	0.2702(4)	0.2704(4)	0.2708(4)	0.2693(4)	0.2702(4)
Y	0.75	0.75	0.75	0.75	0.75	0.75	0.75	0.75
Z	0.0600(7)	0.0596(7)	0.0584(7)	0.0596(7)	0.0602(8)	0.0579(8)	0.0588(8)	0.0575(9)
U_{iso}	0.0083(12)	0.0064(12)	0.0103(11)	0.0098(14)	0.0144(16)	0.0077(14)	0.0105(14)	0.0121(15)
O7X	0.9910(3)	0.9909(4)	0.9903(4)	0.9907(4)	0.9903(4)	0.9905(6)	0.9892(6)	0.9893(6)
Y	0.25	0.25	0.25	0.25	0.25	0.25	0.25	0.25
Z	0.1647(7)	0.1653(7)	0.1662(6)	0.1665(8)	0.1682(9)	0.1683(8)	0.1676(8)	0.1666(9)
U_{iso}	0.0103(13)	0.0091(15)	0.0141(13)	0.0144(16)	0.0153(17)	0.0178(18)	0.0171(18)	0.0185(19)
O8X	0.9969(3)	0.9967(4)	0.9962(4)	0.9962(4)	0.9953(4)	0.9955(4)	0.9961(6)	0.9953(4)
Y	0.75	0.75	0.75	0.75	0.75	0.75	0.75	0.75
Z	0.2938(6)	0.2965(7)	0.2988(6)	0.2999(8)	0.3005(8)	0.3013(8)	0.3018(8)	0.3024(9)
U_{iso}	0.0095(13)	0.0094(14)	0.0135(12)	0.0130(14)	0.0144(17)	0.0117(16)	0.0126(15)	0.0142(17)
O9X	0.4202(4)	0.4200(6)	0.4215(4)	0.4217(4)	0.4204(6)	0.4208(6)	0.4201(6)	0.4207(6)
Y	0.75	0.75	0.75	0.75	0.75	0.75	0.75	0.75
Z	0.4429(8)	0.4446(9)	0.4429(7)	0.4422(9)	0.4463(9)	0.4424(11)	0.4418(11)	0.4431(11)
U_{iso}	0.0189(15)	0.0205(18)	0.0237(16)	0.025(2)	0.025(2)	0.028(2)	0.027(2)	0.028(2)
O10X	0.2677(4)	0.2668(4)	0.2644(4)	0.2633(4)	0.2621(4)	0.2613(4)	0.2620(4)	0.2621(4)
Y	0.25	0.25	0.25	0.25	0.25	0.25	0.25	0.25
Z	0.0743(7)	0.0725(7)	0.0710(7)	0.0679(8)	0.0679(8)	0.0666(8)	0.0667(8)	0.0660(9)
U_{iso}	0.0098(13)	0.0101(14)	0.0142(13)	0.0141(15)	0.0116(15)	0.0101(15)	0.0141(15)	0.0125(16)

Note: *Data measured during decompression.

Table 6. Fitted unit cell parameters, bulk moduli and 1st derivative of the bulk modulus at room-pressure obtained using a BM3 EoS.

	Fe-free				*Fe-rich*			
	a (Å)	*b* (Å)	*c* (Å)	*V* (Å^3)	*a* (Å)	*b* (Å)	*c* (Å)	*V* (Å^3)
Val0	16.2008(8)	5.5530(3)	10.0421(5)	903.39(5)	16.2098(6)	5.5655(2)	10.0536(2)	906.95(5)
K_{T0} (GPa)	244(5)	105.6(1.6)	89.1(9)	122.1(7)	248(4)	106(1)	83.2(5)	119.1(7)
K'	-0.7(1.2)	8.4(5)	6.6(3)	6.8(2)	-0.7(0.9)	8.2(3)	7.5(2)	7.3(2)
Note:								

Formatted: Subscript

Table 7. Linear axial and volume compressibilities (GPa-1) for Fe-free and Fe-rich crystals.

	Fe-free			*Fe-rich*			
	a	*b*	*c*	*a*	*b*	*c*	
K_{T0} (GPa)	244(5)	105.6(1.6)	89.1(9)	248(4)	106(1)	83.2(5)	(a)
Linear modulus (GPa)	732(15)	317(5)	267(3)	744(12)	318(3)	249.60(15)	(b)
Isothermal linear compressibilities (GPa^{-1})	0.00137(3)	0.00314(6)	0.00375(4)	0.00134(2)	0.00314(3)	0.004006(2)	(c)
adiabatic linear compressibilities (GPa^{-1})	0.00132	0.00309	0.00381				(d)

Note: a) This work, K value obtained from EosFit 5.2 using the method described in the text; b) This work, linear modulus, calculated as described in the text; c) This work, Isothermal linear compressibilities, calculated as described in the text; d) Mao et al., (2007), adiabatic linear compressibilities calculated from the sij as described in the text.

Field Code Changed

Table 8. Average rate of change of the distances Al-O (to the shared octahedral edge), Al-Al and O-O (length of the shared edge) distances in zoisite, sillimanite and andalusite.

Formatted: English (U.S.)

	Andalusite			**Sillimanite**			**Zoisite**		
	Label	**Bond distances (room P)**	**rate (Å/GPa)**	**Label**	**Bond distances (room P)**	**rate (Å/GPa)**	**Label**	**Bond distances (room P)**	**rate (Å/GPa)**
Shared edge	**Al1-OA**	1.824(3)	-0.0016	**Al1-OA**	1.916(3)	-0.0074	**M12-O4**	1.841(5)	-0.0005
	Al1-OB	1.893(3)	-0.0013	**Al1-OB**	1.863(3)	-0.0039	**M12-O10**	1.843(5)	-0.0019
							M12-O5	1.901(5)	-0.0041
							M12-O6	1.925(5)	-0.0055
	OA - OA	2.468(7)	-0.0009	**OA - OB**	2.892(8)	-0.0032	**O4-O6**	2.5707(9)	-0.0035
	OA - OA	2.468(7)	-0.0009	**OA - OB**	2.433(8)	-0.0139	**O10-O5**	2.4754(9)	0.0007
Apical oxygen	**Al1-OD**	2.076(3)	-0.0077	**Al1-OD**	1.954(7)	-0.0097	**M12-O1**	1.977(4)	0.0004
							M12-O3	1.862(4)	-0.0037
Al - Al	**Al1-Al1**	2.686(3)	-0.0034	**Al1-Al1**	2.884(0)	-0.0034	**M12-M12**	2.744(4)	-0.0046
	Al1'-Al1'	2.686(3)	0.0070						

Note: Data for sillimanite and andalusite taken from Burt et al., (2004)
The rates of change of the distances are calculated with a linear fit from the length data over the whole pressure range and are recorded as Å/GPa. Atoms labeled as in Figure 1 ~~and Figure 4~~.